Preprints of the 21st IFAC World Congress (Virtual)
Berlin, Germany, July 12-17, 2020

A DFIG-based Wind Turbine Operation under Balanced and Unbalanced Grid Voltage Conditions

Yassine Boukili, A. Pedro Aguiar, and Adriano Carvalho

Department of Electrical and Computer Engineering
Faculty of Engineering, University of Porto (FEUP), Porto, Portugal
{*yassine, pedro.aguiar, asc*}*@fe.up.pt*

Abstract: This paper presents a case study of a Doubly Fed Induction Generator (DFIG) wind turbine in operation subject to balanced and unbalanced grid voltage conditions. Three scenarios are addressed: balanced grid, symmetrical and asymmetrical voltage dips. We describe the DFIG model and the control strategies adopted to stabilize the system during voltage faults, in order to protect the converters. Several simulation experiments are presented to illustrate the performance and effectiveness of the described control strategies.

Keywords: Doubly-fed induction generator (DFIG), Symetrical voltage dips, Asymmetrical voltage dips, DC crowbar protection, control.

1. INTRODUCTION

Nowadays, particular renewable energy resources such as wind based, have already a considerable penetration in the conventional power systems, mainly due to the advances in mechatronics and related fields as well as the increasing (and enforcement) of anti-global warming policies.

With regard to wind power technologies, the Doubly Fed Induction Generator (DFIG) and the permanent magnet synchronous generator share a large part of today's market. Between these two, the DFIG is characterized by some advantages, for instance, the ability to control the active and reactive power by speed variation, and the inexpensive design cost of the DFIG's converter (Ledesma and Usaola, 2005; Zin et al., 2013).

The DFIG has been a subject of intensive research along the years. Some recent results concerning the improvement of the DFIG operation include the simulation of the DFIG and the power quality factor measurement in (Petersson et al., 2005); the control of the active and reactive power in the balanced and the unbalanced voltage of the grid (Xu and Wang, 2007; Erlich et al., 2007; Boukili et al., 2019); the current control for the DFIG using harmonic resonant compensator (Hu et al., 2015); the DFIG inertia improvement in (Aali et al., 2019) by using an adaptive complex least mean square algorithm for frequency estimation; and the improvement of the rotor-side converter operations by using the Fuzzy Logic Controller (Djeridane et al., 2018). Some works also address the enhancement of the DFIG's fault ride-through capability by improving the mathematical model of the DFIG, see e.g., (Rezaei et al., 2012).

A critical problem that arises in the context of the Distributed Energy Resources (DER) when connected to the grid is the unbalanced grid issue that when happens may damage the infrastructure. This area of research is of high importance due to the grid code that imposes the holding of the connection of the DER into the grid even during the grid fault, the so called the Low Voltage Ride Through (LVRT) requirement. The work in (Luo et al., 2019) presents a review of LVRT on DFIG connected into the unbalanced grid. One of the issues is how to insure the stability operation and the protection of the DFIG-based wind turbine during the unbalanced electrical network.

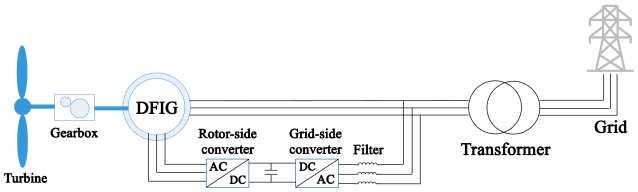

Fig. 1. The Doubly Fed Induction Generator (DFIG) Wind Turbine System.

Recent works with more sophisticated control algorithms have been tackled this problem. In (Ghodbane-Cherif et al., 2019), a deadbeat predictive control method for the rotor side converter is proposed to enhance the behaviour of the wind system under unbalanced grid conditions. The improvement of LVRT capability and the voltage stability by using a new reactive control method is presented in (Gatavi et al., 2019) and by using a crowbar protection in (Kuzhali et al., 2019). A combination of both vector control and direct torque control methods in grid faults, is described in (Jaladi and Sandhu, 2020).

This paper contributes with a study case of a DFIG connected into the electrical network. Three grid states are discussed: balanced grid, symmetrical and asymmetrical voltage dips. We present the modelling, simulation and control of the DFIG shown in Fig. 1. The DFIG diagram is composed by a wind turbine, a gearbox, an asynchronous generator, the stator that is connected directly to the network through a transformer, and the rotor that is connected to the stator through back-to-back converters: the rotor-side converter and the grid-side converter. Several simulation experiments done in Matlab/Simulink are presented to illustrate the performance and effectiveness of the

⋆ This work was supported in part by UID/EEA/00147/2019 - Research Center for Systems and Technologies Unit funded by national funds through the FCT/MCTES through national funds (PIDDAC), project IMPROVE - POCI-01-0145-EDER-031823 and HARMONY - POCI-01-0145-FEDER-031411 funded by FEDER funds through COMPETE2020 – POCI and by national funds (PIDDAC).

described control strategies.
This paper is organized as follows: Section 2 presents the modelling of the wind turbine and the DFIG dynamics. The control method adopted for the DFIG connected into the balanced electrical network is also discussed. Section 3 addresses the unbalanced grid cases. In particular, it presents the symmetrical and asymmetrical voltage dips as well as the controllers adopted for protecting and stabilizing the DFIG operation. Finally, the results obtained are discussed in Section 4.

2. DFIG MODELLING AND CONTROL

This section presents the DIFG model and its control in a balanced electrical network.

2.1 Modelling of the DFIG

In α/β reference frame, the DFIG state space model can be written as (Abad et al., 2011b)

$$\begin{bmatrix}\dot{\psi}_{\alpha s}\\ \dot{\psi}_{\beta s}\\ \dot{\psi}_{\alpha r}\\ \dot{\psi}_{\beta r}\end{bmatrix} = \begin{bmatrix} -\frac{R_s}{\sigma L_s} & 0 & -\frac{R_s L_m}{\sigma L_s L_r} & 0\\ 0 & -\frac{R_s}{\sigma L_s} & 0 & \frac{R_s L_m}{\sigma L_s L_r}\\ \frac{R_r L_m}{\sigma L_s L_r} & 0 & -\frac{R_r}{\sigma L_r} & -\omega_m\\ 0 & \frac{R_r L_m}{\sigma L_s L_r} & \omega_m & -\frac{R_r}{\sigma L_r}\end{bmatrix}\begin{bmatrix}\psi_{\alpha s}\\ \psi_{\beta s}\\ \psi_{\alpha r}\\ \psi_{\beta r}\end{bmatrix} + \begin{bmatrix}V_{\alpha s}\\ V_{\beta s}\\ V_{\alpha r}\\ V_{\beta r}\end{bmatrix}$$

$$\begin{bmatrix}i_{\alpha s}\\ i_{\beta s}\end{bmatrix} = \begin{bmatrix}\frac{1}{\sigma L_s} & 0 & -\frac{L_m}{\sigma L_s L_r} & 0\\ 0 & \frac{1}{\sigma L_s} & 0 & -\frac{L_m}{\sigma L_s L_r}\end{bmatrix}\begin{bmatrix}\psi_{\alpha s}\\ \psi_{\beta s}\\ \psi_{\alpha r}\\ \psi_{\beta r}\end{bmatrix}$$

where ψ is the flux (Wb), V is the voltage (V), i is the current (A), and the sub-indices r and s refer to rotor and stator, respectively. The parameters description can be found in Table 1 and the leakage coefficient of the machine is expressed by

$$\sigma = \frac{(L_r - L_m)^2}{L_r L_s}.$$

From the Newton's second law for a rotational mass, it can be derived that the rotor angular velocity ω_r (rad/s) satisfies (Mensou et al., 2017)

$$\frac{d\omega_r}{dt} = \frac{1}{J}(T_{em} - D\omega_r - T_m),$$

where J is the inertia moment $(kg.m^2)$, T_{em} is the electromagnetic torque $(N.m)$, D is the viscous friction coefficient $(n.s/rad)$, and T_m is the shaft mechanical torque. The torques can be computed from

$$T_{em} = \frac{3}{2}p\frac{L_m}{L_s}(\psi_{qs}i_{dr} - \psi_{ds}i_{qr}), \quad T_m = \frac{P_m}{\omega_r}$$

where p is the number of pole pairs of the machine. The sub-indices d and q in the current i correspond to the two components of the rotating reference frame that results from applying the Park transformation to the two-axis orthogonal stationary reference frame α/β.
To compute the mechanical power, we use (Robinett III and Wilson, 2011)

$$P_m = 0.5\rho A C_p V_w^3$$

where V_w is the wind speed (m/s), ρ is the air density (kg/m^3), A is the rotor swept area (m), and C_p is the power coefficient.

Table 1. The values of the parameters used in the simulation

Parameter	Description	Value
f	Frequency	50 Hz
P_s	Power delivered by the Stator	2×10^6 $Watt$
W_s	Synchronous speed	1500 tr/min
v_s	Stator voltage	690 V
i_s	Stator current	1760 A
T_{em}	Electromechanical torque	12732 $N.m$
p	Number of pole	2
v_r	Rotor voltage	2070 V
R_s	Stator resistance	2.6×10^{-3} Ω
L_s	Stator inductance	2.6×10^{-3} H
L_m	Mutual inductance	2.5×10^{-3} H
R_r	Rotor resistance	2.9 Ω
L_r	Rotor inductance	2.6×10^{-3} H
J	Inertia moment of the rotating parts	127 $Kg.m^2$
D	Coefficient of viscous friction	10^{-3} $n.s/rad$
N	Multiplier coefficient	100
R	Radius of the turbine	42 m
V_{DC}	DC voltage	1150 V
C_{DC}	DC bus capacity	80×10^{-3} F
R_f	Filter resistance	10×10^{-6} Ω
L_f	Filter inductance	200×10^{-6} Ω
R_{cb}	Crowbar resistance	0.2 Ω
ρ	Air density	$1.22 Kg/m^3$

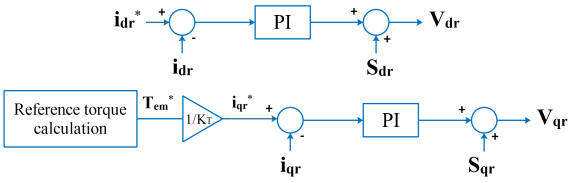

Fig. 2. Rotor-side converter current control loops.

2.2 DFIG control in balanced electrical network

Table 1 presents the values of the variables used in the simulation. The controller objective is to stabilize the DFIG during operation and regulate the DC voltage between the back-to-back converters to a constant value. To this end, the measurement of the following variables are needed: rotor current, stator voltage and current, stator flux, rotor angle, grid current, rotor speed, electromagnetic torque and DC voltage.
The rotor voltage in d/q reference frame, that is deduced from the electrical scheme of the DFIG, can be expressed as

$$V_{dr} = R_r i_{dr} + \sigma L_r \frac{d}{dt} i_{dr} - \omega_r \sigma L_r i_{qr} + \frac{L_m}{L_s}\frac{d}{dt}|\overline{\psi}_s|$$

$$V_{qr} = R_r i_{qr} + \sigma L_r \frac{d}{dt} i_{qr} + \omega_r \sigma L_r i_{dr} + \omega_r \frac{L_m}{L_s}|\overline{\psi}_s|$$

where $\overline{\psi}_s$ denotes the stator flux, expressed in complex notation, that is, $\overline{\psi}_s = \psi_{\alpha s} + j\psi_{\beta s}$. From the above, by commanding in V_{dr} and V_{qr} and applying space vector modulation to control the rotor-side converter, the aim is to regulate the direct rotor current i_{dr} to some desired i_{dr}^* that is proportional to the stator reactive power, and regulate the quadrature rotor current i_{qr} to the desired i_{qr}^* that is proportional to the electromagnetic torque. To obtain i_{qr}^*, a maximum power point tracking (MPPT) method is first used to compute the reference torque $T_{em}^\star$. In this study, we use the indirect control method as MPPT method, see details in (Abad et al., 2011c). Then i_{qr}^* can be deduced from the electromagnetic torque expression

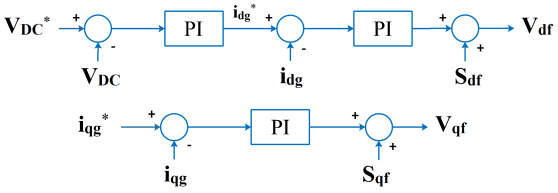

Fig. 3. Grid-side converter control loops.

$$T_{em} = -\frac{3}{2} p \frac{L_m}{L_s} |\overline{\psi}_s| i_{qr} = K_T i_{qr}$$

To obtain the currents and voltages in the d/q reference frame, a Phase Locked-Loop (PLL) is applied to define the angle, that will be used in Park transformation. Fig. 2 shows the control loops of the rotor-side converter. The control law is given by

$$V_{dr} = S_{dr} + k_{p1}\left(i_{dr}^*(t) - i_{dr}(t)\right) + k_{i1}\int_0^t \left(i_{dr}^*(\tau) - i_{dr}(\tau)\right) d\tau$$

$$V_{qr} = S_{qr} + k_{p2}\left(i_{qr}^*(t) - i_{qr}(t)\right) + k_{i2}\int_0^t \left(i_{qr}^*(\tau) - i_{qr}(\tau)\right) d\tau$$

where k_{p1} and k_{p2} are the proportional gains, k_{i1} and k_{i2} are the integral gains, and the feed-forward terms S_{dr} and S_{qr} are

$$S_{dr} = -\omega_r \sigma L_r i_{qr}, \quad S_{qr} = -\omega_r \sigma L_r i_{dr} + \omega_r |\overline{\psi}_s| \frac{L_m}{L_s}$$

To control the grid-side converter, we employ a grid voltage-oriented vector control (GVOVC) approach (Abad et al., 2011a). Let ω_s be the angular speed of the magnetic field, the grid voltage in d/q reference frame can be written as

$$V_{df} = R_f i_{dg} + L_f \frac{di_{dg}}{dt} + V_{dg} - \omega_s L_f i_{qg}$$

$$V_{qf} = R_f i_{qg} + L_f \frac{di_{qg}}{dt} + V_{qg} - \omega_s L_f i_{dg}$$

The aim is to regulate the DC voltage V_{DC} to a constant value by regulating i_{dg}, and control the reactive power exchange with the grid by regulating i_{qg}. Fig. 3 presents the current control loops of this control strategy, where the control signals of the grid-side converters are given by

$$V_{df} = S_{df} + k_{p3}\left(i_{dg}^*(t) - i_{dg}(t)\right) + k_{i3}\int_0^t \left(i_{dg}^*(\tau) - i_{dg}(\tau)\right) d\tau$$

$$V_{qf} = S_{qf} + k_{p4}\left(i_{qg}^*(t) - i_{qg}(t)\right) + k_{i4}\int_0^t \left(i_{qg}^*(\tau) - i_{qg}(\tau)\right) d\tau$$

In the above, k_{p3} and k_{p4} are the proportional gains, k_{i3} and k_{i4} are the integral gains, and S_{df} and S_{qf} are given by

$$S_{df} = -\omega_s L_f i_{qg}, \quad S_{qf} = -\omega_s L_f i_{dg}$$

3. ELECTRICAL NETWORK FAULTS

This section addresses the problem of grid faults, defined as a sudden decrease of amplitude of the voltage grid, or a shift in the three phases angles that can arise due to a problem in the network as a short circuit. In case of unbalanced grid the power electronic equipments used in the microgrid can be damaged if no control protection is carried out. We will now present the two main grid faults, symmetrical and asymmetrical voltage dips.

3.1 Symmetrical voltage dips

Symmetrical voltage dip occurs when the amplitude of the three phases decrease uniformly. In this case, the dip happens directly in the terminals of the DFIG stator, and hence it is important to

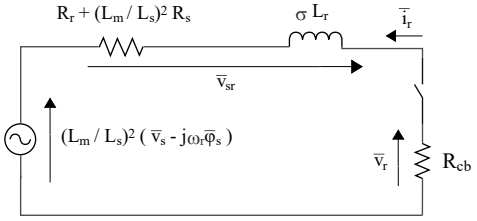

Fig. 4. Equivalent electrical scheme of the DFIG with Crowbar resistance R_{cb}.

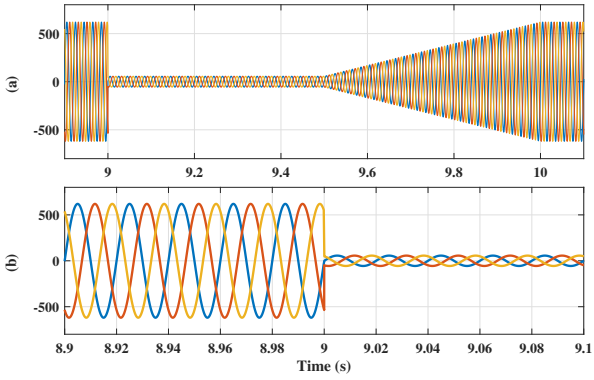

Fig. 5. (a) Grid voltage during the symmetrical voltage dip in V. (b) Zoom in around second 9.

study the stator flux to understand the nature of the fault.
Fig. 4 shows the equivalent electrical scheme of the DFIG where the rotor is referred to the stator. (Abad and Iwanski, 2014). The following equation can be deduced

$$\overline{v}_r = \frac{L_m}{L_s}\left(\overline{v}_s - j\omega_r \overline{\psi}_s\right) + \left[R_r + \left(\frac{L_m}{L_s}\right)^2 R_s\right] \overline{i}_r + \sigma L_r \frac{d}{dt}\overline{i}_r$$

Note also that the variation of the stator flux satisfies (Abad and Iwanski, 2014)

$$\frac{d\overline{\psi}_s}{dt} = \overline{v}_s - \frac{R_s}{L_s}\overline{\psi}_s + R_s \frac{L_m}{L_s}\overline{i}_r$$

where $\overline{v}_r$ is the rotor voltage, $\overline{i}_r$ is the rotor current, $\overline{\psi}_s$ is the stator flux, $\overline{v}_s$ is the stator voltage, and $\overline{i}_s$ is the stator current, where all the variables are expressed in complex notation. When the grid fault occurs, the stator voltage is reduced quickly, and the stator flux cannot follow the variation of the voltage vector. In order to keep $\overline{v}_{sr}$ smaller, the rotor voltage should increase. However, the back-to-back converters are not dimensioned to provide such a large voltage. To mitigate this situation, a crowbar resistance is introduced as shown in Fig. 4. Fig. 5 shows the typical symmetrical dip applied in the simulation, where at the second 9 the voltage is reduced to 10% of the nominal one, instantaneously.
In the simulation, maximum limits of the rotor current and the DC voltage are fixed to detect automatically the grid faults. At the moment that the current or voltage crossover these limits, the crowbar protection will be activated automatically, which will result a fast dumping of the stator flux, implying that most of the energy will go through the crowbar protection, and therefore, the rotor-side converter will be protected. The duration of the crowbar activation is about $100\,ms$, and during this time the control of the rotor-side converter is deactivated. Afterwards, an auxiliary controller takes place to stabilize the DFIG during the voltage dip. This controller is the same as presented in Fig. 2,

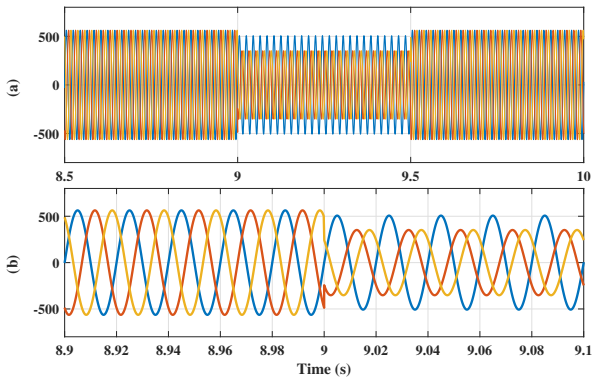

Fig. 6. (a) Grid voltage during the asymmetrical voltage dip in V. (b) Zoom in around second 9.

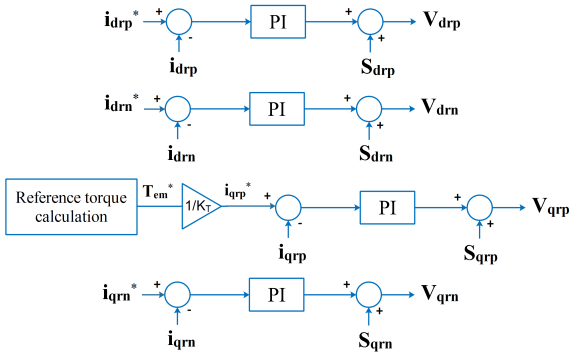

Fig. 7. Dual-vector control loops in the rotor-side converter.

but where the q component of the rotor reference current i^*_{qr} is set to zero, and the reference d component i^*_{dr} is set to a positive value during the grid-fault to provide the given stator reactive power Q_s, that depends on the grid code. From Q_s, we obtain the value of i^*_{dr} using (Abad and Iwanski, 2014)

$$Q_s = -\frac{3}{2}\omega_s \frac{L_m}{L_s}|\overline{\psi}_s|\left(i_{dr} - \frac{|\overline{\psi}_s|}{L_m}\right)$$

3.2 Asymmetrical voltage dips

In some scenarios the grid fault or the non-linear loads can generate asymmetrical voltage dips affecting the DFIG operation and inducing DFIG performance degradation. Fig. 6 presents the case study of asymmetrical voltage dip used in the simulation. In this case, the controller presented in the previous section needs to be re-designed to be able to adequately control the DFIG during the asymmetrical voltage dip. In particular, a common strategy is to apply the Dual vector control approach that adds two more current control loops (see Fig. 7) by decomposing the current references into positive and negative signals (Abad and Iwanski, 2014). The phase-locked loop (PLL) used in this case is synchronized with the positive sequence. In the output of the ABC/dq a notch filter is used to eliminate the coupling sequences that appears at $100\,Hz$. Fig. 7 presents the current loops implemented in the simulations. In the figure, S_{drp} is the d component of the positive cancellation term of the rotor current, S_{drn} is the d component of the negative cancellation term of the rotor current, S_{qrp} is the q component of the positive cancellation term of the rotor current and S_{qrn} is the q component of the negative cancellation term of the rotor current that is,

$$S_{drp} = S_{dr} = -S_{drn}, \quad S_{qrp} = S_{qr} = -S_{qrn}$$

A reference value is given to i^*_{drp} to provide the reactive power in the grid side during the asymmetrical voltage dip, where the values of S_{dgp}, S_{dgn}, S_{qgp} and S_{qgn} are given by

$$S_{dgp} = S_{dg} = -S_{dgn}, \quad S_{qgp} = S_{qg} = -S_{qgn}$$

One can find in the literature several approaches to compute the references of the negative sequences i^*_{drn}, i^*_{qrn}, i^*_{dgn} and i^*_{qgn}. In this work, the balanced rotor currents method (Abad et al., 2011d) is adopted for its simplicity. In this case, all the references are set to zero. Then, the three phases grid current i_g becomes symmetrical.

In the grid-side control, when the asymmetrical grid fault occurs, a reactive power reference has been determined to get a positive value of i^*_{qgp} and a reference value of the DC bus is defined to get the value of i^*_{dgp}. Both positive sequences are needed to obtain the symmetrical three phase grid current i_g with the required amplitude.

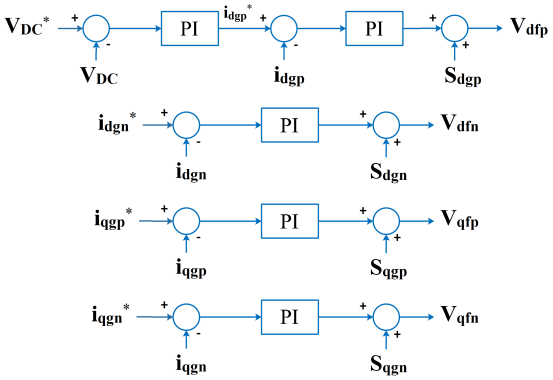

Fig. 8. Dual-vector control loops in the grid-side converter.

4. RESULTS AND DISCUSSION

In this section, the simulation results of the symmetrical and asymmetrical grid faults are presented and discussed. The DFIG simulation is done in Matlab/Simulink. In all the simulations, a wind speed constant value of $8.5\,m/s$ is used, and the rotor speed is set to zero at the time zero.

4.1 Symmetrical voltage dips

The symmetrical voltage dip is applied between the seconds 9 and 10 according to Fig. 5. At the moment of the grid fault, the energy dissipated in the crowbar resistance can be inferred by the current peak that is displayed in Fig. 9 (a). This current peak value can be adjusted according with the value of the crowbar resistance R_{cb}. One can also see that this current vanishes after $100\,ms$. This correspond to the period that the crowbar switch is enabled. During this period plus $20\,ms$ (period that the symmetrical voltage dip controller is still disabled after the crowbar switched off), one can see several perturbations in the signals, namely the rotor currents plotted in Fig. 10. However, once the controller is enabled at the time $t = 9.12\,s$, the q component of the rotor current i_{qr} (see Fig. 10 (b)) is regulated to around zero as desired. Consequently, the electromagnetic torque that in the moment of the fault shows a

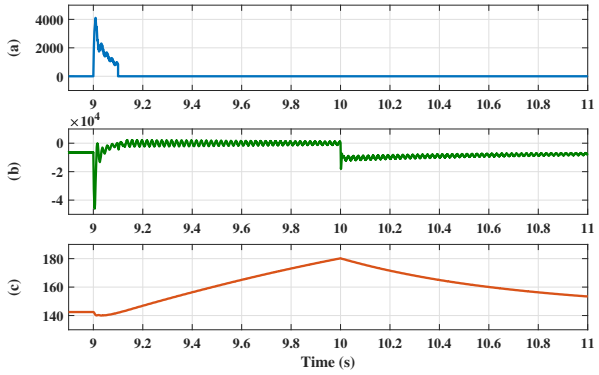

Fig. 9. (a) Crowbar current in A. (b) Electromagnetic torque in $N.m$. (c) Rotor speed during and after the symmetrical voltage dip in rad/s.

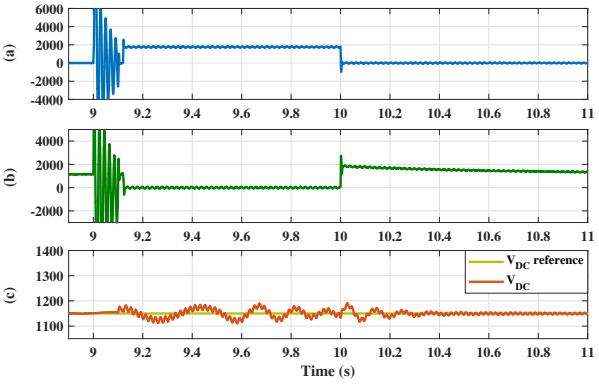

Fig. 10. (a) d component of the rotor current loop control in A. (b) q component of the rotor current loop control in A. (c) DC bus voltage in V.

big peak (that cannot be avoided), also decreases (as expected) to values around zero, but with some small oscillations that are caused by the voltage dip (see Fig. 9 (b)). Unfortunately, the speed of the rotor (see Fig. 9 (c)) is increasing during the fault since it cannot be fully controlled. In a real application, the inertia is chosen higher to reduce the speed increase. Fig. 10 (a) shows the d component of the rotor current control loop that exhibits oscillations during the crowbar activation. Afterwards, it takes a reference value to provide the Grid-side with the adequate reactive power. Regarding the DC bus voltage, Fig. 10 (c) shows that during the grid fault there exist some minor oscillations around the reference value of $1150V$. Note that once the deep voltage cease (second 10), all the signals start to return to their expected normal steady state.

4.2 Asymmetrical voltage dips

The asymmetrical voltage dip is applied between the seconds 9 and 9.5 (see Fig. 6). Similar to the symmetrical voltage dip case, the mechanical speed of the rotor starts to increase during the grid fault because it is not fully controlled. Fig. 11 (a) presents the evolution of the electromagnetic torque that exhibits some oscillations caused by the asymmetrical voltage dip. The oscillations of the torque are mainly because of the grid fault and also due to the negative sequences of the rotor current in d/q components that are fixed to zero. Fig. 11 (b)-(c) present the positive and negative sequences of the rotor

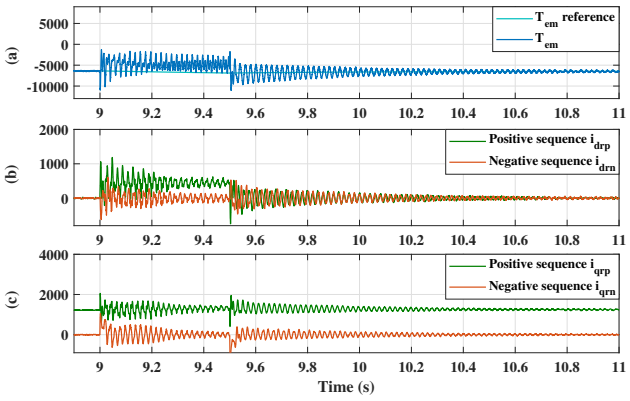

Fig. 11. (a) Electromagnetic torque in $N.m$. (b) Positive and negative sequences of the rotor current d component in A. (c) Positive and negative sequences of the rotor current q component in A.

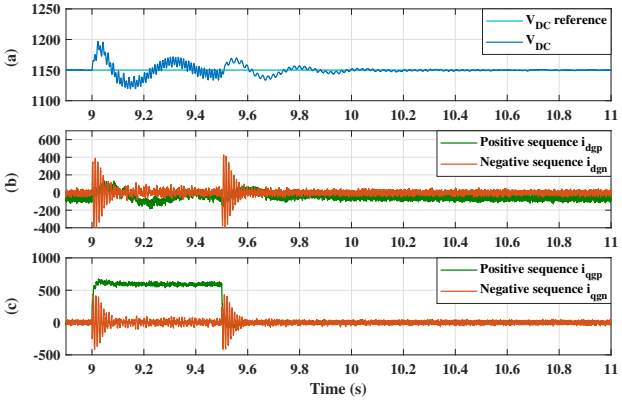

Fig. 12. (a) DC voltage during asymmetrical voltage fault in V, (b) Positive and negative sequences of the grid current d component in A. (c) Positive and negative sequences of the grid current q component in A.

current loops control in d/q reference frame. At the moment of the grid fault (second 9), the current control loops have some perturbations during the transient (that can be eliminated by using a better filter). Overall, we have a quite acceptable performance. The i_{drp} is giving the requested amount of the stator current amplitude. After the grid recovery at the moment $9.5s$ there are some normal perturbations during the transitory period that eventually vanish. Fig. 12 (a), shows the DC voltage during the grid fault with slightly oscillations, but the DFIG can operate normally. Fig. 12 (b)-(c) present the positive and negative sequences of the grid currents loops control in the d/q reference frame. The negative sequences components of the grid current (i_{dgn} and i_{qgn}) are set to zero to make the rotor current symmetric. The current i_{dgp} is making the DC voltage following the reference value $1150V$. A reference value of the reactive power $Q_g^* = -5 \times 10^5 VAR$ is set to provide a positive value of i_{qgp}. The combination of the positive sequences (i_{dgp} and i_{qgp}) is giving the demanded amplitude of the grid control current. The rotor current i_r has perturbations in the beginning of the grid fault, however, the applied controller reduces them significantly as presented in Fig. 13.

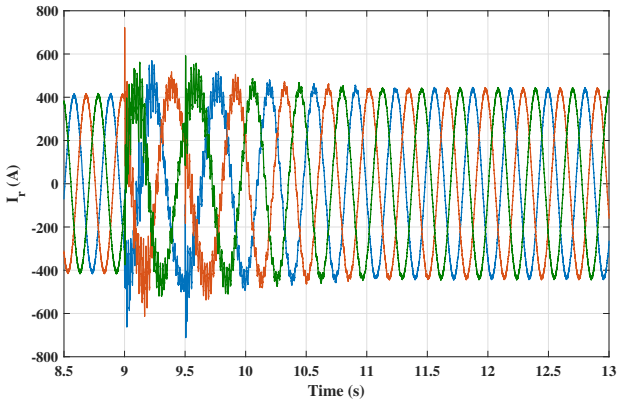

Fig. 13. Three phase rotor currents for the asymmetrical voltage dip case.

5. CONCLUSION

This paper addressed the study of a DFIG-based wind turbine in operation under balanced grid, symmetrical voltage dip, and asymmetrical voltage dip. The control strategies presented to protect the DFIG during grid faults are illustrated through computer simulations. The simulation results show adequate control performance. Future work will include the experimental evaluation of such control strategies.

REFERENCES

Aali, S.R., Besmi, M.R., and Kazemi, M.H. (2019). Adaptive filtering with robust controller for improvement of inertial response of wind turbine. *International Transactions on Electrical Energy Systems*, e12089.

Abad, G. and Iwanski, G. (2014). Properties and control of a doubly fed induction machine. In *Power electronics for renewable energy systems, transportation and industrial applications*, 270–318. Wiley Online Library.

Abad, G., López, J., Rodríguez, M., Marroyo, L., and Iwanski, G. (2011a). Back-to-back power electronic converter. In *Doubly Fed Induction Machine: Modeling and Control for Wind Energy Generation Applications*, 87–154. Wiley Online Library.

Abad, G., López, J., Rodríguez, M., Marroyo, L., and Iwanski, G. (2011b). Dynamic modeling of the doubly fed induction machine. In *Doubly Fed Induction Machine: Modeling and Control for Wind Energy Generation Applications*, 209–239. Wiley Online Library.

Abad, G., López, J., Rodríguez, M., Marroyo, L., and Iwanski, G. (2011c). Introduction to a wind energy generation system. In *Doubly Fed Induction Machine: Modeling and Control for Wind Energy Generation Applications*, 1–85. Wiley Online Library.

Abad, G., López, J., Rodríguez, M., Marroyo, L., and Iwanski, G. (2011d). Vector control strategies for grid-connected dfim wind turbine. In *Doubly Fed Induction Machine: Modeling and Control for Wind Energy Generation Applications*, 303–361. Wiley Online Library.

Boukili, Y., Aguiar, A.P., and Carvalho, A. (2019). Modelling, control and performance evaluation of an ac/dc microgrid. In *IECON 2019-45th Annual Conference of the IEEE Industrial Electronics Society*, volume 1, 2422–2427. IEEE.

Djeridane, M.E., Mechgoug, R., Ajgou, R., and Chemsa, A. (2018). Fuzzy rotor side control of a dfig-based wind turbine. In *2018 International Conference on Communications and Electrical Engineering (ICCEE)*, 1–7. IEEE.

Erlich, I., Kretschmann, J., Fortmann, J., Mueller-Engelhardt, S., and Wrede, H. (2007). Modeling of wind turbines based on doubly-fed induction generators for power system stability studies. *IEEE Transactions on power systems*, 22(3), 909–919.

Gatavi, E., Hellany, A., Nagrial, M., and Rizk, J. (2019). Advanced reactive power control strategy for better lvrt capability for dfig-based wind farm. In *2019 IEEE International Conference on Environment and Electrical Engineering and 2019 IEEE Industrial and Commercial Power Systems Europe (EEEIC/I&CPS Europe)*, 1–6. IEEE.

Ghodbane-Cherif, M., Skander-Mustapha, S., and Slama-Belkhodja, I. (2019). An improved predictive control for parallel grid-connected doubly fed induction generator-based wind systems under unbalanced grid conditions. *Wind Engineering*, 0309524X19858253.

Hu, J., Huang, Y., Wang, D., Yuan, H., and Yuan, X. (2015). Modeling of grid-connected dfig-based wind turbines for dc-link voltage stability analysis. *IEEE Transactions on Sustainable Energy*, 6(4), 1325–1336.

Jaladi, K.K. and Sandhu, K.S. (2020). Real-time simulator based hybrid controller of dfig-wes during grid faults design and analysis. *International Journal of Electrical Power & Energy Systems*, 116, 105545.

Kuzhali, M., Isac, S.J., and Poongothai, S. (2019). Improvement of low voltage ride through capability of grid-connected dfig wts using fuzzy logic controller. In *International Conference on Intelligent Computing and Applications*, 349–359. Springer.

Ledesma, P. and Usaola, J. (2005). Doubly fed induction generator model for transient stability analysis. *IEEE transactions on energy conversion*, 20(2), 388–397.

Luo, J., Zhao, H., Lu, X., Gao, S., Ma, Q., and Terzija, V. (2019). A review of low voltage ride through in dfig under unbalanced grid faults. In *2019 IEEE PES GTD Grand International Conference and Exposition Asia (GTD Asia)*, 718–723. IEEE.

Mensou, S., Essadki, A., Nasser, T., and Idrissi, B.B. (2017). An efficient nonlinear backstepping controller approach of a wind power generation system based on a dfig. *International Journal of Renewable Energy Research*, 7(4), 1520–1528.

Petersson, A., Thiringer, T., Harnefors, L., and Petru, T. (2005). Modeling and experimental verification of grid interaction of a dfig wind turbine. *IEEE Transactions on Energy Conversion*, 20(4), 878–886.

Rezaei, E., Tabesh, A., and Ebrahimi, M. (2012). Dynamic model and control of dfig wind energy systems based on power transfer matrix. *IEEE Transactions on Power Delivery*, 27(3), 1485–1493.

Robinett III, R.D. and Wilson, D.G. (2011). *Nonlinear power flow control design: utilizing exergy, entropy, static and dynamic stability, and Lyapunov analysis*. Springer Science & Business Media.

Xu, L. and Wang, Y. (2007). Dynamic modeling and control of dfig-based wind turbines under unbalanced network conditions. *IEEE Transactions on Power Systems*, 22(1), 314–323.

Zin, A.A.B.M., HA, M.P., Khairuddin, A.B., Jahanshaloo, L., and Shariati, O. (2013). An overview on doubly fed induction generators controls and contributions to wind based electricity generation. *Renewable and Sustainable Energy Reviews*, 27, 692–708.